Extending the limits of Pt/C catalysts with passivation-gas-incorporated atomic layer deposition

Shicheng Xu, [1]

Yongmin Kim, [1]

Joonsuk Park, [2]

Drew Higgins, [3]

Shih-Jia Shen, [4]

Peter Schindler, [5]

Dickson Thian, [6]

J. Provine, [5]

Jan Torgersen, [1,7]

Tanja Graf, [8]

Thomas D. Schladt, [8]

Marat Orazov, [3]

Bernard Haochih Liu, [4]

Thomas F. Jaramillo, [3]

Fritz B. Prinz, [1✉,2,7]

Email fprinz@stanford.edu

[1] Department of Mechanical Engineering, Stanford University, Stanford, CA, USA

[2] Department of Material Science and Engineering, Stanford University, Stanford, CA, USA

[3] Department of Chemical Engineering, Stanford University, Stanford, CA, USA

4 Department of Materials Science and Engineering, National Cheng Kung University, Tainan, Taiwan

5 Department of Electrical Engineering, Stanford University, Stanford, CA, USA

6 Department of Applied Physics, Stanford University, Stanford, CA, USA

7 Department of Mechanical and Industrial Engineering, Norwegian University of Science and Technology, Trondheim, Norway

8 Volkswagen Group Research, Wolfsburg, Germany

Received: 5 January 2018 / Accepted: 4 July 2018

Abstract

Controlling the morphology of noble metal nanoparticles during surface depositions is strongly influenced by precursor–substrate and precursor–deposit interactions. Depositions can be improved through a variety of means, including tailoring the surface energy of a substrate to improve precursor wettability, or by modifying the surface energy of the deposits themselves. Here, we show that carbon monoxide can be used as a passivation gas during atomic layer deposition to modify the surface energy of already deposited Pt nanoparticles to assist direct deposition onto a carbon catalyst support. The passivation process promotes two-dimensional growth leading to Pt nanoparticles with suppressed thicknesses and a more than 40% improvement in Pt surface-to-volume ratio. This approach to synthesizing nanoparticulate Pt/C catalysts achieved high Pt mass activities for the oxygen reduction reaction, along with excellent stability likely facilitated by strong catalyst–support interactions afforded by this synthetic technique.

AQ1

The synthesis of nanocatalysts with small dimensions and high surface-to-volume ratios is of great interest to lower catalyst costs and exploit catalytic performance enhancements through size effects. Now, Prinz and colleagues show that two-dimensional growth of platinum nanoparticles with suppressed thicknesses can be promoted with passivation-gas-incorporated atomic layer deposition.

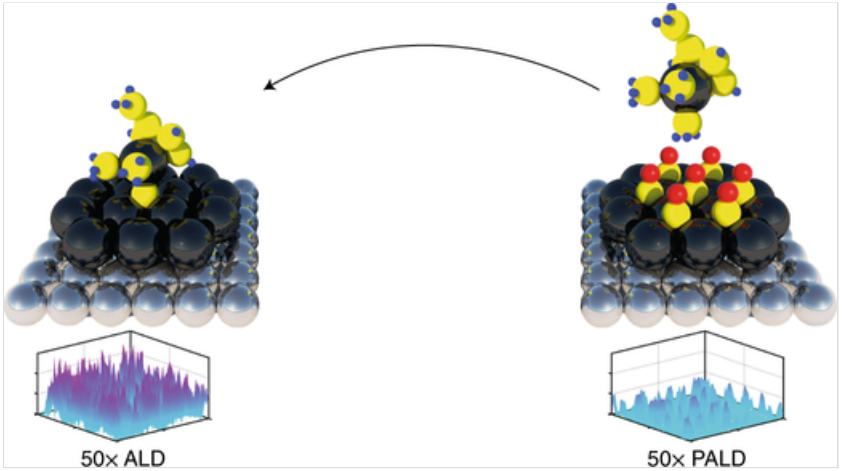

Main

Heterogeneous catalysis is a surface process involving only a few layers of atoms at or near the catalyst surface. For precious metal catalysts, the synthesis of nanostructures with such small dimensions is of great interest to lower catalyst costs and exploit catalytic performance enhancements through size effects. For example, we can consider Pt-based catalysts for the oxygen reduction reaction (ORR); inefficient catalysts for this reaction serve as the primary factor limiting the performance of low-temperature polymer electrolyte fuel cells (PEFCs)[1, 2]. Small nanoparticles are desired to maximize Pt utilization and an optimal diameter of 2–3 nm (ref. [3, 4, 5]) has been found to result in the highest mass activity for solid Pt nanoparticles. While smaller particles <2 nm offer a greater fraction of exposed Pt atoms at the surface, they also exhibit a higher proportion of under-coordinated surface sites[6, 7] which bind oxygen-containing reaction intermediates too strongly[8, 9], leading to low specific activity (on a surface area basis). Structures such as nanowires[10, 11, 12] and nanoframes[13] with confined dimensions have been previously explored, demonstrating different size and morphological effects on the catalytic performance largely based on aiming to achieve high surface areas while maintaining high specific activity.

AQ2

AQ3

AQ4

The controlled synthesis of nanostructures with confined dimensions can be achieved in a variety of ways, for instance the use of encapsulating ligands[13, 14, 15] that restrain growth in certain dimensions or using templates that allow for materials to be deposited in a controllable manner, such as electrochemical deposition[16, 17, 18]. The former method usually requires a subsequent transfer process in which ligand-capped catalysts are dispersed onto a catalyst support. By contrast, the direct growth of catalysts on a support surface is possible using templates that are pre-bonded to the support[19, 20, 21]. Such processes usually result in either core–shell or hollow structures, by either retaining the template as the core material or by removing the template, respectively. Core materials are designed to improve the initial catalytic performance, but the

dissolution of core metal ions during fuel cell operation may lead to undesired performance loss[22, 23]. In this work, we explore another approach, controlling the morphology of Pt during its direct deposition onto the support in the absence of any templates. Through improved direct chemical bonding of Pt on the underlying catalyst support, we aim to improve both the activity and the stability of such catalyst structures.

Atomic layer deposition (ALD) is a promising approach for the direct deposition of Pt onto catalyst supports. Due to its ability to conformally coat high-surface-area substrates, ALD has gained growing attention in a number of technological areas, including heterogeneous catalysis[24, 25, 26]. For the case of ORR in particular, ALD has been used to fabricate Pt-based catalysts on various support materials, such as carbon nanotubes[27, 28, 29], metal oxides (including TiO_2 (ref. [30]), SiO_2 (ref. [31]) and $LiCoO_2$ (ref. [32])) and various metal carbides[33] and silicides[34]. Despite the wide array of substrates that have been used, the deposition of very thin Pt layers or clusters with ALD remains a challenge, which has limited the resulting Pt-based mass activity. This challenge is primarily attributed to the nucleation delay that is often associated with noble metal ALD processes, where nanoparticles grow not only laterally but vertically to a certain height before covering the entire substrate. This behaviour is not unique to ALD but is also encountered in other techniques, including templated electrochemical deposition[35]. Inhibitors have been applied to hinder accumulated growth using chemical vapour deposition[36, 37]. For electrochemical deposition of Pt, hydrogen[38, 39] and carbon monoxide[40, 41] have been used to limit the dimensions of Pt particles; however, catalysts with appropriately tailored structures and dimensions that are useful for the ORR are yet to be achieved.

In this report, we explore using carbon monoxide as a growth inhibitor during ALD to achieve the direct deposition of ultrathin Pt nanoparticles onto carbon substrates. Using this technique, carbon monoxide strongly adsorbs on the deposited Pt surface, passivating it from subsequent Pt precursor adsorption. As a result, two-dimensional growth of Pt nanoparticles can be realized, a process we refer to as passivation-gas-incorporated ALD (PALD). The PALD deposition of Pt on glassy carbon (GC) results in >40% improvement in Pt-based mass activity for the ORR compared with similar catalysts prepared by normal ALD. The PALD approach was also successfully translated to a nanostructured carbon powder, yielding catalysts demonstrating a high mass activity exceeding 1 A mg_{Pt}^{-1} @ 0.9 V versus a reversible hydrogen electrode (RHE), as well as providing excellent electrochemical stability probably due to the improved direct bonding between Pt nanoparticles and the carbon support.

Results

Thickness suppression with PALD

With conventional ALD, the growth of noble metals, such as Pt, typically undergoes a nucleation delay, where the vertical and horizontal growth of the deposited materials continue steadily with increasing substrate surface coverage until a complete film has been formed. This behaviour is due to a difference in the adsorption energetics of the precursors onto either the already deposited materials or the original substrate. As illustrated in Fig. 1a, Pt precursor molecules more readily adsorb onto deposits that have already been formed through previous ALD cycles[42]. An effective strategy to mitigate growth of the already nucleated phase while promoting precursor coverage on the substrate is to choose a substrate with a high surface energy to favour precursor adsorption[43]. However, this strategy imposes fundamental restrictions on the types of substrates that can be employed. To overcome this limitation, we developed an alternative strategy that includes the use of CO as a passivation gas. This PALD process is illustrated in Fig. 1b, where the deposited Pt layer surface is modified by CO adsorbates to passivate the Pt atoms from preferential precursor adsorption during subsequent cycles. This phenomenon is illustrated by our model of a Pt(111) slab covered by a complete

monolayer of Pt. In this CO-passivated case, the platinum precursor, methylcyclopentadienyltrimethylplatinum ($MeCpPtMe_3$), has a considerably lower adsorption energy (Supplementary Table 1) on CO-passivated Pt compared with that on bare Pt. This lower affinity for adsorption onto CO-passivated Pt deposits thus increases the probability of precursor wetting the bare substrate regions.

Fig. 1

Pt nanoparticle growth with ALD and PALD.

a,**b**, Schematics of the ALD (**a**) and PALD (**b**) processes compared in the precursor adsorption stage. **c**–**j**, STEM-EELS annular dark-field micrographs (**c**–**f**) and 3D views of relative thickness mappings (**g**–**j**) on 25 and 50 cycles of ALD versus 50 and 75 cycles of PALD deposited on thin carbon films.

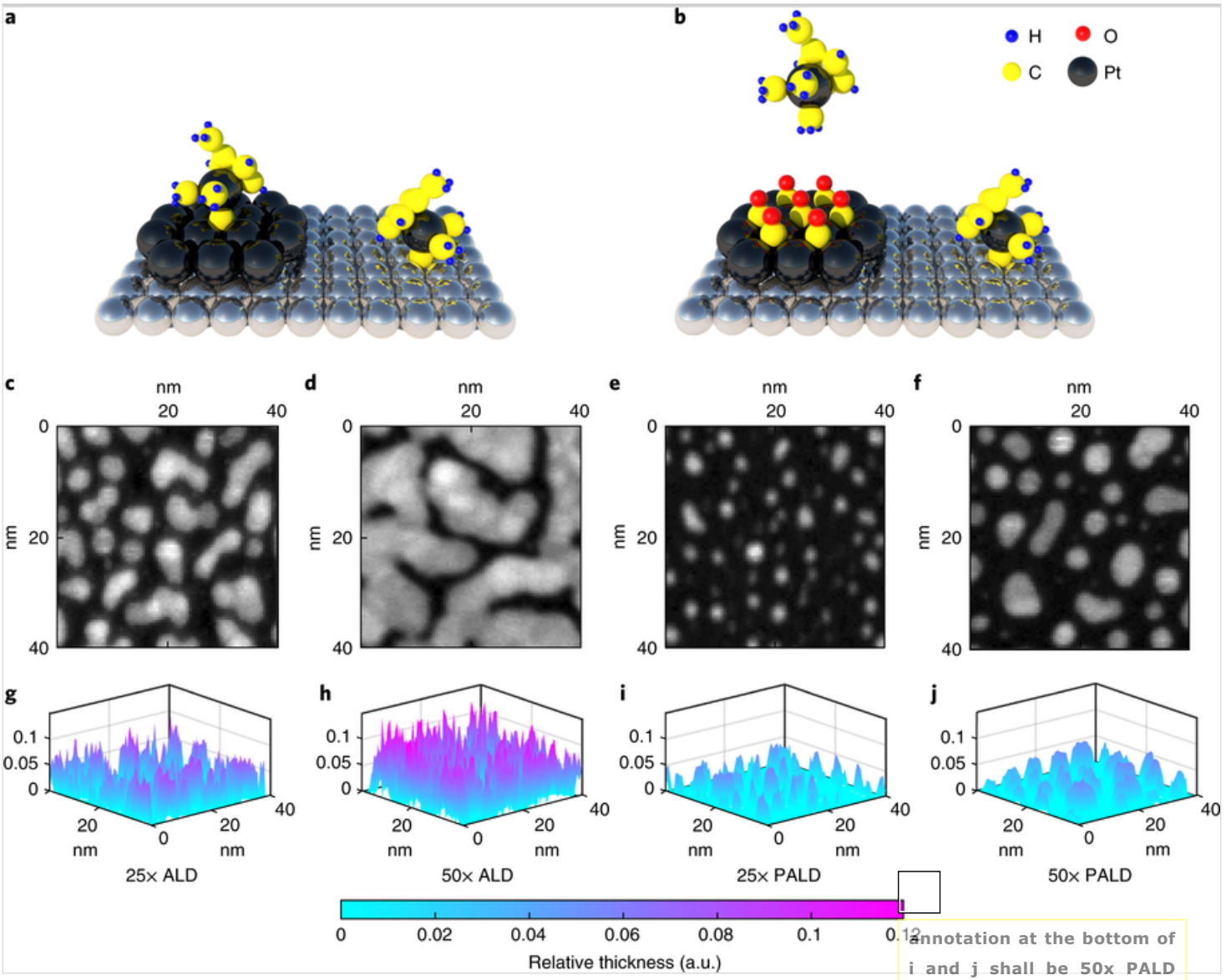

annotation at the bottom of i and j shall be 50x PALD and 75x PALD, respectively. Apologies for making this mistake when updating the figure. Please correct that it is consistent with the caption.

Figure 1 shows top-view scanning transmission electron microscopy (STEM) images of Pt deposits by ALD (Fig. 1c,d) and PALD (Fig. 1e,f) onto a flat carbon thin film (~3 nm, RMS roughness 0.2 nm), along with 3D maps showing the relative thickness, in units of the inelastic mean free path, of the Pt deposits as measured by electron energy loss spectroscopy (EELS). The ALD data pertain to 25 (Fig. 1c) and 50 (Fig. 1d) cycles, whereas the PALD data pertain to 50 (Fig. 1e) and 75 (Fig. 1f) cycles. Two effects can be seen when comparing the two processes: (1) the overall deposition rate of PALD is much slower than that of ALD, given the noticeably lower loading for the PALD samples despite the greater number of

deposition cycles compared to ALD, and (2) PALD yields a much more lateral growth compared to ALD. In the ALD process, increasing the number of cycles by 25, from 25 to 50, yields a substantial growth in both the horizontal and vertical directions. However, in the PALD process, increasing the number of cycles by 25, from 50 to 75, leads to particles that have grown wider (lateral growth) but not noticeably taller. The PALD particles after 50 cycles and 75 cycles are of very similar heights, an average height differential of only 12%. In contrast, the average height differential is 43% between the ALD particles of 25 and 50 cycles. The STEM and EELS data in Fig. 1 allow for average particle height–width profiles to be constructed for each of the four samples (Supplementary Fig. 1). With normal ALD, the average particle clearly increases in both height and width when increasing the number of cycles by 25, indicating both lateral and vertical growth. In PALD, lateral growth is the dominant growth mode. One can also compare ALD versus PALD by examining particles of similar average lateral dimensions, 25 cycles of ALD compared to 75 cycles of PALD; while the particle width is nearly identical in both cases, the PALD particles are substantially flatter. At a similar Pt loading, the 10 cycles of ALD and 50 cycles of PALD result in different particle width, height and density. Similar comparison applied to the 20 cycles of ALD and 75 cycles of PALD (Supplementary Fig. 2). These data confirm our hypotheses that PALD can provide more flat nanoparticle geometries compared to ALD, as well as suppressed growth rates.

Catalytic activity of ALD and PALD Pt nanoparticles

As PALD allows for improved Pt dispersion on carbon supports by means of reduced particle thickness, we used this method to synthesize Pt catalysts for ORR catalysis, aiming to improve Pt mass activity (MA). Pt was directly deposited by both PALD and ALD onto GC electrodes to investigate electrochemical activity using a rotating disc electrode (RDE) setup. GC serves as a model substrate due to its low background ORR activity, relatively low degree of defects and chemical functionality and a planar geometry that encounters less mass transport impedance compared with high-surface-area carbon. It also has an amorphous carbon surface similar to that of the carbon thin film used in the STEM-EELS measurement. The Pt mass loadings for the synthesized catalysts are shown as a function of the cycle number for both normal ALD and PALD in Fig. 2a. In good agreement with the findings on the STEM-EELS thickness mapping, passivation with CO during PALD synthesis decreases the Pt deposition rate on GC, by at least a factor of five. Catalysis measurements are presented in Fig. 2b, exhibiting Pt-based MA values (A mg_{Pt}^{-1}) measured at 0.9 V versus RHE as a function of mass loading ($\mu g_{Pt}\ cm^{-2}$) for both ALD and PALD samples. For normal ALD, the highest MA achieved within the explored synthesis range is 0.9 A mg_{Pt}^{-1}, a respectable value that exceeds United States Department of Energy performance targets for 2020 (0.44 A mg_{Pt}^{-1}). The MA of the Pt catalysts prepared by PALD, however, are far superior, particularly at mass loadings below 3 $\mu g_{Pt}\ cm^{-2}$ where the highest MA of PALD Pt particles exceeded 1.3 A mg_{Pt}^{-1}, reflecting an improvement of >40% compared to ALD.

Fig. 2

Comparing ORR activities of PALD and ALD Pt nanoparticles.

a, Mass loadings of Pt deposition via ALD (blue) and PALD (red) as a function of the cycle number. **b**–**d**, MA (**b**), ECA (**c**) and SA (**d**) of ALD and PALD samples for ORR as a function of mass loading. The activity measurements were obtained at 0.9 V versus RHE. The average values and error bars were obtained as the standard deviation of measurements from five replicate samples.

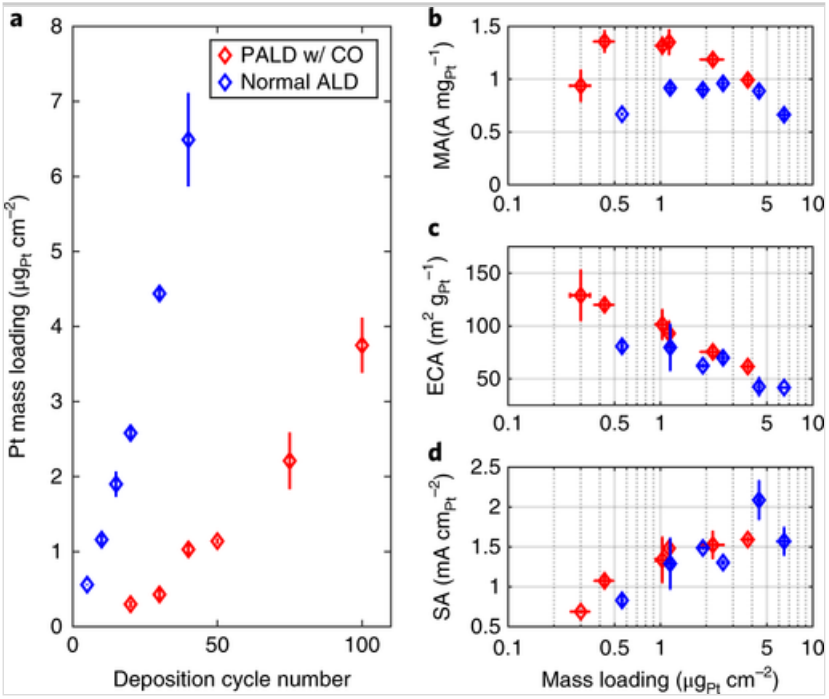

We attribute the improved MA of the Pt particles prepared by PALD to the more appropriate, flatter nanoparticle morphology achieved by using a passivating gas compared to the Pt particles prepared by normal ALD. Figure 2c,d provides additional insights, revealing trends in electrochemically active area (ECA, $m^2\ g_{Pt}^{-1}$) and specific activity (SA, mA cm_{Pt}^{-2} measured at 0.9 V versus RHE), respectively, as a function of mass loading ($\mu g_{Pt}\ cm^{-2}$). Figure 2c shows that for both ALD and PALD, the ECA decreases with increased mass loading, as expected. Important to note is that for a given mass loading, the ECA of the PALD catalysts is greater than that of the ALD catalysts; this reflects that for a given mass loading, PALD yields a morphology in which more Pt atoms are exposed to the electrolyte, boding well for greater Pt utilization for ORR catalysis. Figure 2d shows another important effect. Indeed, as expected, SA increases with higher mass loadings for both ALD and PALD samples due to increased particle sizes and thus fewer proportionate under-coordinated sites as described earlier[6, 7]. Comparing ALD to PALD, particularly in the region of lower mass loading, it shows that for a given mass loading the SA of the PALD samples is higher than that for ALD. This is probably the result of fewer proportionate under-coordinated sites in the PALD samples, another indicator of a flatter morphology. This morphology engenders a higher ECA and SA for the PALD samples compared to those prepared by ALD; these two factors combine to produce catalysts with significantly higher MA for the PALD samples.

To study the geometries of these particles in detail, atomic force microscopy (AFM) studies were conducted (Fig. 3) in addition to the STEM-EELS measurements described earlier. Although STEM-EELS provides excellent, atomic-level lateral resolution, the thickness mapping (as shown in Fig. 1) can only yield relative values. Conversely, AFM can provide excellent resolution in the vertical direction on an absolute scale, albeit with lateral resolution and accuracy limited by the AFM tip shape. Therefore, we applied both complementary techniques to provide a more

thorough probe of the geometries of the Pt nanoparticles. AFM is particularly effective on samples that are nearly atomically flat; we found that GC was too rough (RMS roughness of 1.9 nm) for the quantitative measurements we desired and thus used AFM to investigate Pt deposited on ultra-flat silicon dioxide thin films. The growth rate of Pt on silicon dioxide is lower than that of Pt on amorphous carbon. Nevertheless, given both samples of study are in the island growth regime where the vertical growth of the particle is dominated by the precursor–deposit interactions[44, 45], the differences in the wettability of SiO_2 and carbon are not so significant as to prevent a meaningful comparison of the nanoparticles, as can be observed by comparing the data in Fig. 3 and Fig. 1. We chose 50 cycles of PALD and 20 cycles of ALD for a comparative study, given that these cycle numbers correspond to the peak ORR MA for each series. With 50 cycles of PALD, particles are smaller and sparsely distributed. By contrast, 20 cycles of ALD yield particles that are larger and more closely packed. The average cross-sectional profiles of the two samples suggest that 50 cycles of PALD yields particles with an average height of approx. 1.2 nm and that the particles from 20 cycles of ALD are taller with an average height of approx. 1.6 nm. The average diameter of the particles prepared by 20 ALD cycles is also 5 nm larger than that prepared by 50 cycles of PALD. Modelled as particles with a spherical cap shape, the surface area to volume ratio of the 50-cycle PALD particles are approximately 35-40% larger than the 20-cycle ALD particles. These ratios agree with the ECA values (on a mass basis) shown in Fig. 2c, with an average value of 93 $m^2\ g_{Pt}^{-1}$ for 50 cycles of PALD and 70 $m^2\ g_{Pt}^{-1}$ for 20 cycles of ALD. This further highlights the considerable enhancement in MA for the ORR that can be attributed to a higher portion of surface atoms available for catalysis when preparing thin layers of Pt nanoparticles by PALD.

Fig. 3

Morphological difference between best-performing ALD and PALD Pt nanoparticles.

a–**c**, AFM images with 3D morphologies of 20 cycles of ALD (**a**), 50 cycles of PALD (**b**) and a comparative view of their average cross-sectional profiles (**c**). The scale bars in the AFM images represent 20 nm. The average values and error bars were obtained as the standard deviation of eleven randomly picked line profiles (centre aligned) of each sample.

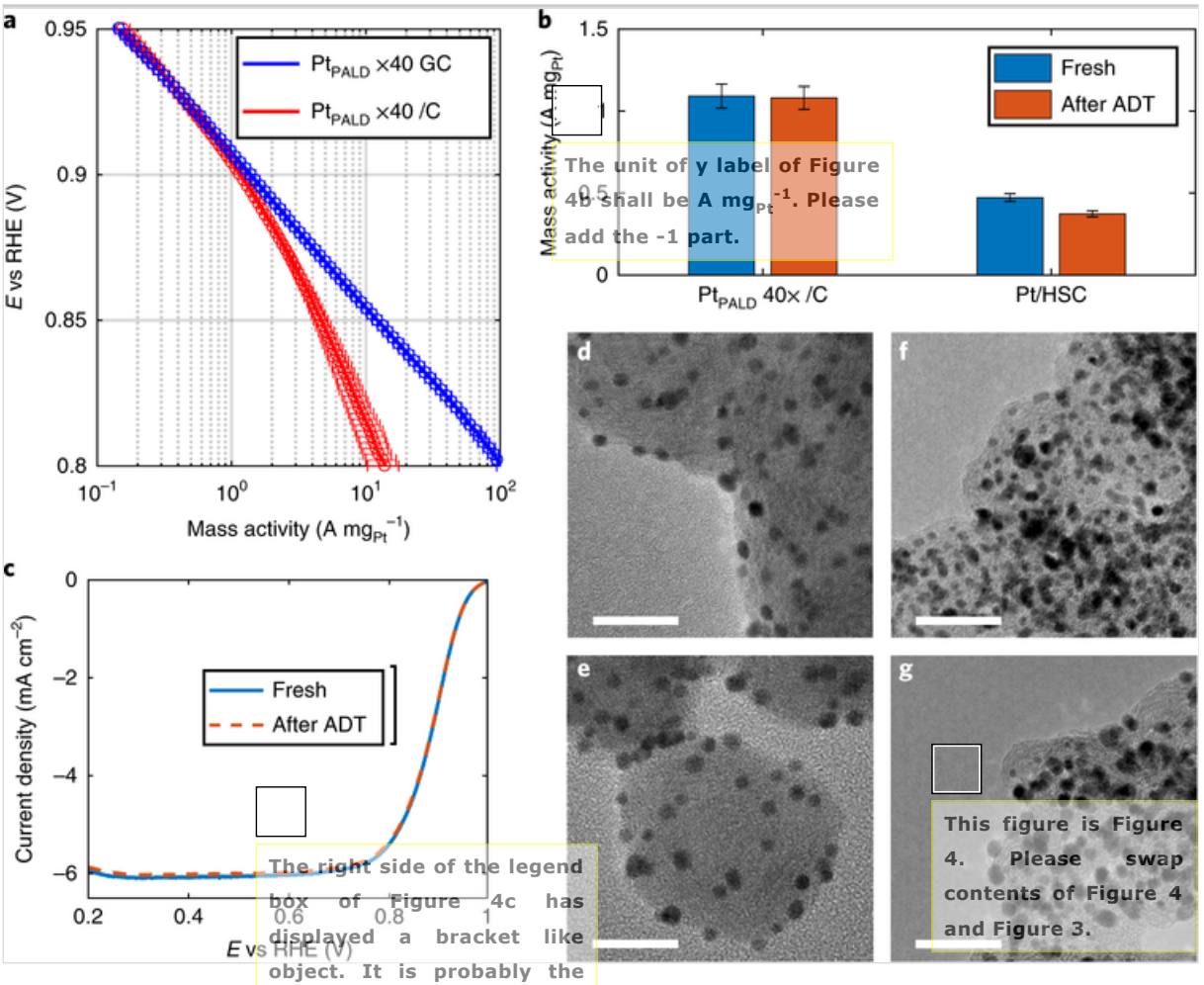

The unit of y label of Figure 4b shall be A mg_{Pt}^{-1}. Please add the -1 part.

The right side of the legend box of Figure 4c has displayed a bracket like object. It is probably the uncovered part of the legend in the underlying figure. Please slightly move or enlarge the legend box so that the bracket is not shown.

This figure is Figure 4. Please swap contents of Figure 4 and Figure 3.

Catalytic performance of Pt/C catalysts synthesized by PALD

To demonstrate the feasibility of fabricating practical carbon-powder-supported Pt catalysts with this technique, PALD was performed on commercial carbon powders. These Pt_{PALD}/C powdered materials were then formulated into an electrocatalyst ink and cast onto GC electrodes to evaluate their activities. The average mass activities of the Pt_{PALD}/C powder catalysts and the thin-layer Pt_{PALD} nanoparticles on GC (Pt_{PALD}/GC) are compared in Fig. 4a. Concentration corrections[46] were performed to exclude underestimation of the performances of Pt_{PALD}/C catalysts due to their higher loading than their GC-supported counterparts (7 μg_{Pt} cm^{-2} versus 1 μg_{Pt} cm^{-2}). As shown by the different mass activities between Pt on flat GC and 3D carbon powder (Fig. 4a), mass transport impedance plays a significant role on the Pt/C samples due to nanostructuring and the presence of Nafion, as clearly indicated by a widened discrepancy between the Pt_{PALD}/C and Pt_{PALD}/GC samples below 0.9 V (versus RHE). The Tafel plots overlapped almost exactly at electrochemical potentials above 0.92 V (versus RHE), where the current density is mostly kinetically

dominated. The MA of the Pt_{PALD}/C catalyst at 0.9 V versus RHE is 1.16 A mg_{Pt}^{-1}, more than double that of the commercial Pt on high surface area carbon catalyst (Pt/HSC) as shown by Fig. 4b.

Fig. 4

Activity and stability of Pt/C catalysts synthesized with PALD.

a, Mass activity as a function of electrochemical potential for a GC electrode and carbon powder decorated with 40 cycles of PALD. The average values and error bars were obtained as the standard deviation of measurements from three replicate samples at a loading around 7 $\mu g_{Pt}\,cm^{-2}$. **b**, Mass activity of Pt_{PALD} 40×/C and a commercial Pt/HSC catalyst before and after ADT. The average values and error bars were obtained as the standard deviation of measurements from at least three replicate samples (evaluation loading ~~@~~at 4–8 $\mu g_{Pt}\,cm^{-2}$ for Pt_{PALD} 40×/C and 8–10 $\mu g_{Pt}\,cm^{-2}$ for Pt/HSC). **c**, ORR polarization curves of ~~Pt/C with 40 cycles of PALD (~~Pt_{PALD} 40×/C~~)~~ before and after 10,000 cycles (0.6 to 1.0 V versus RHE) of an ADT in O_2-saturated electrolyte. **d**–**g**, Pt particle morphologies examined by TEM before (**d** for Pt_{PALD} 40×/C and **f** for Pt/HSC) for and after (e for Pt_{PALD} 40×/C and **g** for Pt/HSC) the ADT test. The scale bars represent 20 nm.

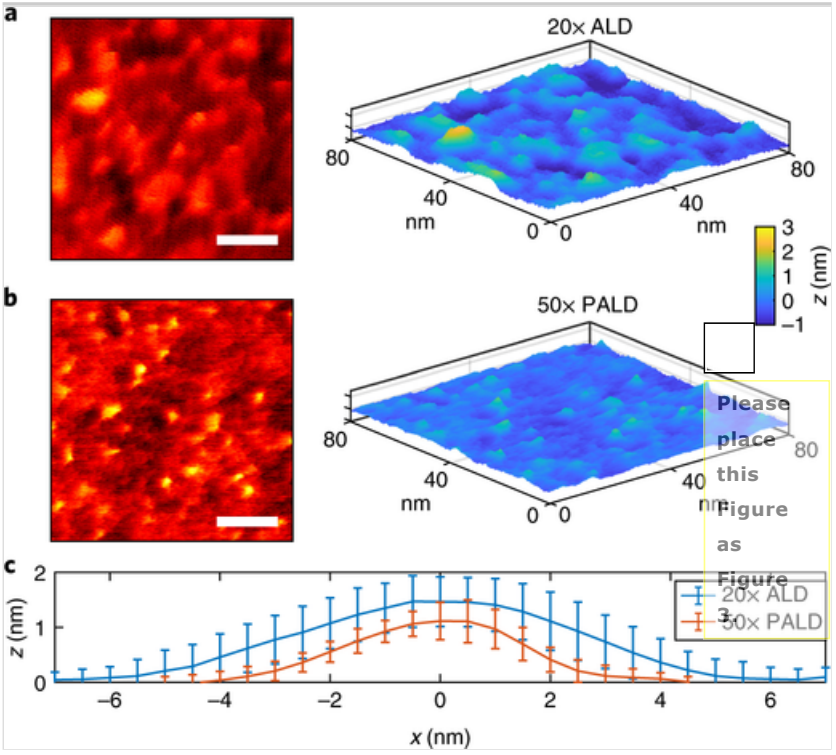

The electrochemical stability of the catalyst was evaluated by an accelerated degradation test (ADT) by cycling between 0.6 and 1.0 V (versus RHE) in an O_2-saturated electrolyte and measuring ORR polarization curves before and after this process, as shown in Fig. 4c. Only a minor

(10%) loss in the ECA was observed (cyclic voltammetry data in Supplementary Fig. 3) along with a nearly overlapping ORR activity measured following this ADT. This activity retention was found to coincide with minimal morphology changes to the Pt_{PALD}/C catalyst after 10,000 cycles of the ADT. The same ADT protocol was applied to the Pt/HSC catalyst, the loss of kinetic current density of Pt/HSC mounts to 21% with an ECA decrease of 14% after 10,000 cycles. TEM imaging is shown in Fig. 4c,d, indicating that the Pt nanoparticles produced by PALD retained an average diameter of 3.1 nm and that only a slight ripening occurred, as evidenced from the increased standard deviation of the equivalent diameter from 0.5 nm to 0.7 nm (compare with Supplementary Fig. 4). By contrast, an obvious increase in particle diameter (from 2.5 ± 1.2 nm to 3.3 ± 1.9 nm) can be noticed with Pt/HSC. This outstanding catalyst stability of Pt_{PALD}/C can be attributed to a number of factors. On the one hand, smaller Pt particle variation and respective interparticle distances with Pt_{PALD}/C (as compared with the Pt/HSC catalysts in Fig. 4f and Supplementary Fig. 5) make the particles less prone to Ostwald ripening and coalescence. On the other hand, the defect-initiated growth mechanism of ALD can possibly lead to strong Pt–support interactions as implied by the adhesive energy calculations in Supplementary Fig. 6.

In summary, we have demonstrated the use of a passivation gas to suppress the thickness of nanoparticles deposited during ALD. This PALD technique enabled the direct deposition of thinner Pt nanoparticles onto carbon-based catalyst supports, which enabled greater Pt utilization due to a more suitable nanoparticle morphology. This combination of effects allowed for the PALD Pt/C catalysts to achieve a twofold increase in the mass activity for ORR compared to a commercial Pt/C catalyst. The PALD Pt/C catalyst also demonstrated excellent stability following 10,000 cycles of an accelerated durability test. To further push the limit of surface-to-volume ratio of Pt particles with PALD, precursor and oxidant chemistry can be carefully designed to curb surface diffusion[47] and formation of oxide intermediates. With a better understanding of the adsorbate–adsorbent structures with in situ characterization techniques such as FTIR[48], the surface chemistry can be better elucidated and passivation gases tailored to precursor chemistries can be developed. It is expected that the versatile chemical capabilities of ALD can lead to the development of new catalyst structures that had been challenging to synthesize and integrate. The recent rapid development in spatial ALD reactors[49, 50] can make it an emerging technique for commercial-scale materials synthesis.

Methods

PALD and ALD

ALD of Pt was achieved by alternately exposing the Pt precursor, trimethyl(methylcyclopentadienyl) Pt(IV) (ref. [51]) ($MeCpPtMe_3$, 99%, Strem Chemicals), and the oxidant ozone[52] to target substrates (carbon TEM grid, GC electrode and carbon powder). Ozone was generated from oxygen (99.99%) mixed with nitrogen (99.998%) with a mixing concentration of about 50 ppm in an ozone generator (MKS Instruments, AX8407-C2). The feeding oxygen flow rate was kept at about 500 sccm, providing an ozone concentration of about 21.7 wt%. The Pt precursor was heated to approximately 80 °C. The substrate temperature was kept at 120 °C. Pt precursor was first introduced to the chamber with a 1 s pulse followed by a 3 s soak and the same exposure time was used for the ozone dosage. To ensure the formation of metallic Pt, hydrogen[53, 54] (99.999%, Praxair) was introduced in each cycle at 1 torr for 25 s after the oxidation stage to remove oxide species[55].

PALD was achieved by incorporating a passivation gas soaking step at the end of each ALD cycle. In this study, carbon monoxide (99.5%, Praxair) was fed into the ALD chamber to soak the substrate at 2 torr for 20 s at the end of each ALD cycle. The substrate temperature ensures respectful surface coverage of CO on the deposited Pt (refs. [56, 57, 58]). Prior to Pt deposition, the carbon substrates underwent an exposure to oxygen plasma in a plasma cleaner (Harrick PDC-001, 30 W) for 10 min for surface functionalization.

Electrochemical measurement

For ORR activity tests, Pt-coated GC electrodes were assembled in RDE tips. The electrolyte was diluted from 70% perchloric acid (Merck, Suprapur) to 0.1 mol l^{-1} with ultrapure water (18.2 MΩ·cm, TOC < 5 ppb). A three-electrode cell was used with a platinum wire as the counter electrode and RHE as the reference electrode. During ORR measurements, the pressure of oxygen was balanced by the atmospheric pressure. The measurement temperature was 23 ± 2 °C, and the voltammetry was conducted by the Gamry PCI4/300 potentiostat. To minimize contaminants, all glassware was soaked in piranha solution for more than 24 h and rinsed five times with ultrapure water prior to use. Before measuring their ORR activities, all electrodes underwent an activation process in argon-gas-purged electrolyte with cyclic voltammetry from 0.025 V to 1.0 V for 50 cycles at a scan rate of 500 mV s^{-1} under an electrode rotation speed of 2,500 r.p.m. ORR activity of the catalyst-loaded electrode was evaluated by a linear sweep voltammetry at a scan rate of 20 mV s^{-1} from –0.01 V to 1 V under an electrode rotation speed of 1,600 r.p.m. All reported values are corrected by subtracting the background and uncompensated electrolyte resistance.

For Pt_{PALD}/C catalysts, 45 mg of carbon powder (based on mass of carbon) was dispersed in 25 ml ultrapure water to assist sonication. 3 ml of the suspension was further diluted threefold with ultrapure water, followed by addition of 10 µl of 5% Nafion 117 solution (Aldrich) and 1.12 ml of anhydrous ethanol (≥99.5%, Sigma-Aldrich). This mixture was then sonicated in an ice bath for 20 min prior to dispersion onto GC electrodes. For a typical electrode, an aliquot of 10–40 µl is dropped to the RDE tip (corresponding Pt loading range from 2 to 20 µg cm^{-2}), which was rotated at 700 r.p.m. for 1 h for solvent evaporation and thin film formation. The electrode is then measured with the same protocol as described above. For the Pt/HSC catalysts, inks were prepared by mixing 7.6 mg Pt/HSC catalyst powder (TEC10E50E, 46.6 wt%) with 7.6 ml deionized water, 2.4 ml isopropanol (≥99.7%, Aldrich) and 40 µl of 5 wt% Nafion solution[59]. Following the same rotational air drying method as described above, the RDE tip was prepared for measurement.

ADT was conducted by cycling the electrochemical potential from 0.6 V to 1.0 V (versus RHE) with a scan rate of 100 mV s^{-1} for 10,000 cycles. After ADT (roughly 23 h), electrolyte was replaced and the same activation and cyclic voltammetry processes in the inert gas saturated environment were conducted before performing test of ORR activity ~~testing~~.

Material characterization

Mass of Pt was quantified by inductively coupled plasma mass spectrometry. For Pt/C samples, the electrode was immersed in aqua regia overnight, and the Pt concentration of the solution was measured. For Pt on GC electrodes, the backside and side walls of the electrodes were first polished before soaking in aqua regia.

Morphological studies were performed with STEM-EELS and AFM. For STEM-EELS-based thickness mappings, Pt was deposited on ultrathin carbon film (~3 nm) supported by a lacey carbon film on a 400 mesh copper grid (Ted Pella) using ALD and PALD. The 3-nm-thick supported amorphous carbon film was chosen for its low surface roughness and amorphous surface with C–O termination. A spherical aberration-corrected TEM (FEI Titan TEM 80–300) operating at 80 kV in scanning mode had been utilized for obtaining STEM-EELS spectra. The TEM was equipped with a Gatan Quantum EEL spectrometer.

EELS spectra were acquired using a camera length of 38 mm and a spectrometer entrance aperture of 2.5 mm, providing a convergence semi-angle of 9.9 mrad and a collection semi-angle of 25.9 mrad. A STEM dark-field image and STEM-EELS map were obtained in the region of interest with a window size of 50 nm × 50 nm with the setting of 0.5 nm EELS step size, 0.05 s exposure time, 0.4 eV ch^{-1} dispersion and a reflective tail method for zero loss peak subtraction.

A procedure obtaining relative thickness maps is summarized as follows (Supplementary Fig. 7): First, annular dark-field images were collected for particle recognition and differentiating thickness profiles of Pt particles from the bare carbon background. It has been known as relative thickness $\boldsymbol{t/\lambda = \ln(I_t/I_0)}$ where I_t and I_0 are the total and zero loss regions from the obtained STEM-EELS spectra and λ is the total inelastic mean free path of an electron at 80 kV (ref. [60]). The particles are not highly oriented and mostly polycrystalline. It is assumed that possible variations of electron mean free path due to local packing density differences do not significantly affect the thickness measurement results sampled over these polycrystalline particles.

Morphologies of samples made with PALD and ALD are also studied by an AFM (Bruker Dimension ICON, Bruker). Considering the roughness of GC and ultrathin carbon film on TEM, we deposited Pt on to 200 nm thermally grown amorphous silicon oxide film on an ultra-flat silicon wafer with low roughness 2–3 Å (Ted Pella). The samples with 20 × ALD and 50 × PALD were compared as they correspond to highest catalytic performance in either recipe.

Due to the nature of the nanoparticle formation, low-noise sub-nanometre spatial (x–y) resolution and sub-angstrom height (z) resolution are required. The AFM system was set on an anti-vibration marble slab with active air cushion for reduction of environmental disturbances. Furthermore, the AFM was enclosed in a custom-made, temperature and humidity-controlled Faraday cage to maintain a consistent measurement environment of 25 ± 1 °C and <10% relative humidity, and to block any electromagnetic stray signals. Before AFM measurements, the sample surface was gently blown by dry nitrogen gas (Research Purity, 99.998%, YunSun Special Gases) for 10 min to remove dust and surface humidity. The scan parameters were carefully adjusted to minimize the noise level before the actual data acquisition began. Because the goal is to capture nanoparticles as small as possible, an advanced AFM scan mode (Peak Force Tapping) that utilized a non-resonant feedback scheme was adopted to achieve high image resolution at minimal (~10 pN) tip–sample interaction force. A brand-new ultra-sharp AFM probe (SAA-HPI-SS, Bruker) with a nominal tip end radius of 1 nm and cantilever spring constant of 0.25 N m^{-1} was used for each AFM measurement to effectively avoid possible image quality degradation due to tip wear.

Due to the nature of tip–sample interaction, the AFM images inevitably contain the physical profile of the AFM tip in use[61]. The real surface morphology image of a specimen has to be reconstructed by removing the known tip shape from the acquired AFM image, an image processing technique called ‘tip deconvolution’. This is especially important for our specimen as the expected nanoparticle size was comparable to that of the ultra-sharp AFM probe used for the measurements. The three-dimensional tip shape profile was characterized by scanning the tip on a TipCheck calibration sample (NioProbe, Aurora NanoDevices) with numerous tiny sharp peaks (<5 nm) and the AFM tip apex profile was estimated by the blind tip image reconstruction algorithm[62, 63].

In the current study, sample 50 × PALD was measured by tip 1, while 20 × ALD was scanned by tip 2. Both tip 1 and tip 2 were brand new for the first scan on an individual sample. After the AFM measurements were complete, tip 1 and tip 2 were brought to scan the TipCheck calibration

sample to access their 3D profile (Supplementary Table 2). Third party image processing software (Gwyddion, Czech Metrology Institute) was used to perform tip deconvolution of the AFM images. Tip deconvolution 1 was processed by directly using the known tip shape from TipCheck; the evaluated tip radius for 50 × PALD/tip 1 was 4.5 nm and for 20 × ALD/tip 2 was 5.6 nm. Tip deconvolution 2 was processed based on the correction of tip apex half angle which was smaller than the image processing software considered. An overestimated tip half angle may result in over-cutting of surface extrusion profile thus a sharper and rougher morphology. Both tip 1 and tip 2 became to have effective tip radii of ~7 nm based on tip deconvolution 2. The effects of tip deconvolution with the examples of the 50 × PALD and 20 × ALD samples are shown in Supplementary Tables 3 and 4, respectively. Figure 3 presents tip deconvolution 1.

Density functional theory calculation

The adsorption energy of precursor onto Pt- and CO-passivated Pt clusters was calculated by density functional theory with the package QUANTUM ESPRESSO[64]. The Perdew–Burke–Ernzerhof exchange–correlation functional and norm-conserving pseudopotentials were used to describe core electron interactions. The Kohn–Sham one-electron valence states were expanded in a plane wave basis set with a kinetic energy cutoff of 35 Ry, which is sufficient for energy convergence. A monolayer 3 × 3 Pt (111) slab employing a 5 × 5 × 1 *k*-point grid was selected for accommodating a $MeCpPtMe_3$ precursor molecule. The zero-temperature chemical adsorption energy was calculated by the energy difference between when the precursor molecule is placed far away from the slab and when the precursor molecule is right on top of the slab. All calculated states had undergone ionic relaxations with energy convergence. The adhesion energy between a 4 × 4 graphene surface and a $Pt_7(111)$ cluster was obtained by the energy difference of an isolated slab-surface bonded structure and the combination of those of insolated slab and surfaces, normalized by the number of Pt atoms on the surface.

Data availability

The authors declare that the data supporting the findings of this study are available within the paper and its Supplementary Information. Extra data are available from the corresponding author upon reasonable request.

Electronic supplementary material

Supplementary information is available for this paper at https://doi.org/10.1038/s41929-018-0118-1.

Publisher's note: Springer Nature remains neutral with regard to jurisdictional claims in published maps and institutional affiliations.

Acknowledgements

This work was supported financially by the Volkswagen Group of America. Part of this work was performed at the Stanford Nano Shared Facilities (SNSF), supported by the National Science Foundation under award ECCS-1542152. S.X. thanks support from and discussions with L. Johal, G. Li, Z. Lu and Y. Liu. D.H. acknowledges support from the Banting Postdoctoral Fellowship, administered by the government of Canada. J.T. acknowledges funding from the Austrian Science Fund (FWF) under contract J3505-N20. P.S. acknowledges financial support from the Austrian Science Fund (FWF) under contract J3980-N27.

Author contributions

S.X. conceived the PALD process and conducted the initial feasibility tests with P.S., D.T., J.Pr. and J.T. under the supervision of F.B.P.; S.X., Y.K. and D.H. tested catalytic performance of PALD-deposited Pt under the supervision of F.B.P. and T.F.J.; S.X., J.Pa., D.T., S.S. and B.H.L. performed material characterizations and analysed the data; S.X., D.H., M.O., J.Pr., Y.K., T.G., T.D.S., T.F.J. and F.B.P. wrote the manuscript.

Competing interests The authors declare no competing interests.

Supplementary information

Supplementary Information

Supplementary Figures 1–14, Supplementary Tables 1–4, Supplementary References

References

1. Debe, M. K. Electrocatalyst approaches and challenges for automotive fuel cells. *Nature* **486**, 43–51 (2012).

2. Kongkanand, A. & Mathias, M. F. The priority and challenge of high-power performance of low-platinum proton-exchange membrane fuel cells. *J. Phys. Chem. Lett.* **7**, 1127–1137 (2016).

3. Shao, M., Peles, A. & Shoemaker, K. Electrocatalysis on platinum nanoparticles: particle size effect on oxygen reduction reaction activity. *Nano Lett.* **11**, 3714–3719 (2011).

4. Nesselberger, M. et al. The particle size effect on the oxygen reduction reaction activity of pt catalysts: influence of electrolyte and relation to single crystal models. *J. Am. Chem. Soc.* **133**, 17428–17433 (2011).

5. Perez-Alonso, F. J. et al. The effect of size on the oxygen electroreduction activity of mass-selected platinum nanoparticles. *Angew. Chem. Int. Ed.* **51**, 4641–4643 (2012).

6. Zhang, J., Yang, H., Fang, J. & Zou, S. Synthesis and oxygen reduction activity of shape-controlled Pt_3Ni nanopolyhedra. *Nano Lett.* **10**, 638–644 (2010).

7. Wang, J. X. et al. Oxygen reduction on well-defined core-shell nanocatalysts: particle size, facet, and Pt shell thickness effects. *J. Am. Chem. Soc.* **131**, 17298–17302 (2009).

8. Stephens, I. E. L., Bondarenko, A. S., Grønbjerg, U., Rossmeisl, J. & Chorkendorff, I. Understanding the electrocatalysis of oxygen reduction on platinum and its alloys. *Energy Environ. Sci.* **5**, 6744 (2012).

9. Nørskov, J. K. et al. Origin of the overpotential for oxygen reduction at a fuel-cell cathode. *J. Phys. Chem. B* **108**, 17886–17892 (2004).

10. Li, M. et al. Ultrafine jagged platinum nanowires enable ultrahigh mass activity for the oxygen reduction reaction. *Science* **354**, 1414–1419 (2016).

11. Jiang, K. et al. Efficient oxygen reduction catalysis by subnanometer Pt alloy nanowires. *Sci. Adv*. **3**, e1601705 (2017).

12. Higgins, D. C. et al. Morphology and composition controlled platinum-cobalt alloy nanowires prepared by electrospinning as oxygen reduction catalyst. *Nano Energy* **10**, 135–143 (2014).

13. Chen, C. et al. Highly crystalline multimetallic nanoframes with three-dimensional electrocatalytic surfaces. *Science* **343**, 1339–1343 (2014).

14. Zhang, L. et al. Platinum-based nanocages with subnanometer-thick walls and well-defined, controllable facets. *Science* **349**, 412–416 (2015).

15. Duan, H. et al. Ultrathin rhodium nanosheets. *Nat. Commun.* **5**, 3093 (2014).

16. Wang, J. X. et al. Kirkendall effect and lattice contraction in nanocatalysts: a new strategy to enhance sustainable activity. *J. Am. Chem. Soc.* **133**, 13551–13557 (2011).

17. Adzic, R. R. et al. Platinum monolayer fuel cell electrocatalysts. *Top. Catal.* **46**, 249–262 (2007).

18. Herrero, E., Buller, L. J. & Abruña, H. D. Underpotential deposition at single crystal surfaces of Au, Pt, Ag and other materials. *Chem. Rev.* **101**, 1897–1930 (2001).

19. Wang, J. X. et al. Oxygen reduction on well-defined core-shell nanocatalysts: Particle size, facet, and Pt shell thickness effects. *J. Am. Chem. Soc.* **131**, 17299–17302 (2009).

20. Zhang, Y. et al. High performance Pt monolayer catalysts produced via core-catalyzed coating in ethanol. *ACS Catal.* **4**, 738–742 (2014).

21. Zhang, J. et al. Platinum monolayer electrocatalysts for O_2 reduction: Pt monolayer on Pd(111) and on carbon-supported Pd nanoparticles. *J. Phys. Chem. B* **108**, 10955–10964 (2004).

22. Sasaki, K. et al. Core-protected platinum monolayer shell high-stability electrocatalysts for fuel-cell cathodes. *Angew. Chem. Int. Ed.* **49**, 8602–8607 (2010).

23. Okada, T. Theory for water management in membranes for polymer electrolyte fuel cells. Part 2. The effect of impurity ions at the cathode side on the membrane performances. *J. Electroanal. Chem.* **465**, 18–29 (1999).

24. Singh, J. A., Yang, N. & Bent, S. F. Nanoengineering heterogeneous catalysts by atomic layer deposition. *Annu. Rev. Chem. Biomol. Eng.* **8**, 41–62 (2017).

25. O'Neill, B. J. et al. Catalyst design with atomic layer deposition. *ACS Catal.* **5**, 1804–1825 (2015).

26. Lu, J. et al. Coking- and sintering-resistant palladium catalysts achieved through atomic layer deposition. *Science* **335**, 1205–1208 (2012).

27. Cheng, N. et al. High stability and activity of Pt electrocatalyst on atomic layer deposited metal oxide/nitrogen-doped graphene hybrid support. *Int. J. Hydrog. Energy* **39**, 15967–15974 (2014).

28. Chen, Y. et al. Atomic layer deposition assisted Pt-SnO_2 hybrid catalysts on nitrogen-doped CNTs with enhanced electrocatalytic activities for low temperature fuel cells. *Int. J. Hydrog. Energy* **36**, 11085–11092 (2011).

29. Cheng, N. et al. Extremely stable platinum nanoparticles encapsulated in a zirconia nanocage by area-selective atomic layer deposition for the oxygen reduction reaction. *Adv. Mater.* **27**, 277–281 (2015).

30. Du, Q., Wu, J. & Yang, H. Pt@Nb-TiO_2 catalyst membranes fabricated by electrospinning and atomic layer deposition. *ACS Catal.* **4**, 144–151 (2014).

31. Inaba, M., Suzuki, T., Hatanaka, T. & Morimoto, Y. Fabrication and cell analysis of a Pt/SiO_2 platinum thin film electrode. *J. Electrochem. Soc.* **162**, F634–F638 (2015).

32. Wang, H. et al. Direct and continuous strain control of catalysts with tunable battery electrode materials. *Science* **354**, 1031–1036 (2016).

33. Cheng, N. et al. Atomic scale enhancement of metal–support interactions between Pt and ZrC for highly stable electrocatalysts. *Energy Environ. Sci.* **8**, 1450–1455 (2015).

34. Xie, J., Yang, X., Han, B., Shao-Horn, Y. & Wang, D. Site-selective deposition of twinned platinum nanoparticles on $TiSi_2$ nanonets by atomic layer deposition and their oxygen reduction activities. *ACS Nano* **7**, 6337–6345 (2013).

35. Shao, M., Chang, Q., Dodelet, J.-P. & Chenitz, R. Recent advances in electrocatalysts for oxygen reduction reaction. *Chem. Rev.* **116**, 3594–3657 (2016).

36. Liao, W. & Ekerdt, J. G. Effect of CO on Ru nucleation and ultra-smooth thin film growth by chemical vapor deposition at low temperature. *Chem. Mater.* **25**, 1793–1799 (2013).

37. Babar, S. et al. Growth inhibitor to homogenize nucleation and obtain smooth HfB_2 thin films by chemical vapor deposition. *Chem. Mater.* **25**, 662–667 (2013).

38. Liu, Y., Gokcen, D., Bertocci, U. & Moffat, T. P. Self-terminating growth of platinum films by electrochemical deposition. *Science* **338**, 1327–1330 (2012).

39. Nutariya, J., Fayette, M., Dimitrov, N. & Vasiljevic, N. Growth of Pt by surface limited redox replacement of underpotentially deposited hydrogen. *Electrochim. Acta* **112**, 813–823 (2013).

40. Wang, H., Jiang, K., Chen, Q., Xie, Z. & Cai, W.-B. Carbon monoxide mediated chemical deposition of Pt or Pd quasi-monolayer on Au surfaces with superior electrocatalysis for ethanol oxidation in alkaline media. *Chem. Commun.* **52**, 374–377 (2016).

41. Brimaud, S. & Behm, R. J. Electrodeposition of a Pt monolayer film: using kinetic limitations for atomic layer epitaxy. *J. Am. Chem. Soc.* **135**, 11716–11719 (2013).

42. Novak, S., Lee, B., Yang, X. & Misra, V. Platinum nanoparticles grown by atomic layer deposition for charge storage memory applications. *J. Electrochem. Soc.* **157**, H589 (2010).

43. Baker, L. et al. Growth of continuous and ultrathin platinum films on tungsten adhesion layers using atomic layer deposition techniques. *Appl. Phys. Lett.* **101**, 111601 (2012).

44. Puurunen, R. L. & Vandervorst, W. Island growth as a growth mode in atomic layer deposition: a phenomenological model. *J. Appl. Phys.* **96**, 7686–7695 (2004).

45. Lee, H. B. R. & Bent, S. F. Formation of continuous Pt films on the graphite surface by atomic layer deposition with reactive O_3. *Chem. Mater.* **27**, 6802–6809 (2015).

46. Xu, S. et al. Building upon the Koutecky-Levich equation for evaluation of next-generation oxygen reduction reaction catalysts. *Electrochim. Acta* **255**, 99–108 (2017).

47. Dendooven, J. et al. Independent tuning of size and coverage of supported Pt nanoparticles using atomic layer deposition. *Nat. Commun.* **8**, 1074 (2017).

48. Bosch, R. H. E. C., Bloksma, F. L., Huijs, J. M. M., Verheijen, M. A. & Kessels, W. M. M. Surface infrared spectroscopy during low temperature growth of supported Pt nanoparticles by atomic layer deposition. *J. Phys. Chem. C* **120**, 750–755 (2016).

49. Hoye, R. L. Z. et al. Research update: atmospheric pressure spatial atomic layer deposition of ZnO thin films: reactors, doping, and devices. *APL Mater.* **3**, 40701 (2015).

50. Longrie, D.., Deduytsche, D.., & Detavernier, C.. Reactor concepts for atomic layer deposition on agitated particles: a review. *J. Vac. Sci. Technol. A* **32**, 10802 (2014).

51. Aaltonen, T., Ritala, M., Sajavaara, T., Keinonen, J. & Leskelä, M. Atomic layer deposition of platinum thin films. *Chem. Mater.* **15**, 1924–1928 (2003).

52. Dendooven, J. et al. Low-temperature atomic layer deposition of platinum using (methylcyclopentadienyl)trimethylplatinum and ozone. *J. Phys. Chem. C* **117**, 20557–20561 (2013).

53. Setthapun, W. et al. Genesis and evolution of surface species during Pt atomic layer deposition on oxide supports characterized by in situ XAFS analysis and water−gas shift reaction. *J. Phys. Chem. C* **114**, 9758–9771 (2010).

54. MacKus, A. J. M., Garcia-Alonso, D., Knoops, H. C. M., Bol, A. A. & Kessels, W. M. M. Room-temperature atomic layer deposition of platinum. *Chem. Mater.* **25**, 1769–1774 (2013).

55. Hämäläinen, J., Puukilainen, E., Sajavaara, T., Ritala, M. & Leskelä, M. Low temperature atomic layer deposition of noble metals using ozone and molecular hydrogen as reactants. *Thin Solid Films* **531**, 243–250 (2013).

56. Rupprechter, G., Dellwig, T., Unterhalt, H. & Freund, H. J. High-pressure carbon monoxide adsorption on Pt(111) revisited: a sum frequency generation study. *J. Phys. Chem. B* **105**, 3797–3802 (2001).

57. Steininger, H., Lehwald, S. & Ibach, H. On the adsorption of CO on Pt(111). *Surf. Sci.* **123**, 264–282 (1982).

58. Primet, M., Basset, J. M., Mathieu, M. V. & Prettre, M. Infrared study of CO adsorbed on Pt Al_2O_3. A method for determining metal-adsorbate interactions. *J. Catal.* **29**, 213–223 (1973).

59. Shinozaki, K., Zack, J. W., Pylypenko, S., Pivovar, B. S. & Kocha, S. S. Oxygen reduction reaction measurements on platinum electrocatalysts utilizing rotating disk electrode technique: II. Influence of ink formulation, catalyst layer uniformity and thickness. *J. Electrochem. Soc.* **162**, F1384–F1396 (2015).

60. Malis, T., Cheng, S. C. & Egerton, R. F. EELS log-ratio technique for specimen-thickness measurement in the TEM. *J. Electron Microsc. Tech.* **8**, 193–200 (1988).

61. Liu, H.-C., Osborne, J. R., Osborn, M. & Dahlen, G. A. Advanced CD-AFM probe tip shape characterization for metrology accuracy and throughput. In *Proc. SPIE* (ed. Archie, C. N.) 65183K (2007).

62. Villarrubia, J. S. Algorithms for scanned probe microscope image simulation, surface reconstruction, and tip estimation. *J. Res. Natl Inst. Stand. Technol.* **102**, 425 (1997).

63. Qian, X. & Villarrubia, J. S. General three-dimensional image simulation and surface reconstruction in scanning probe microscopy using a dexel representation. *Ultramicroscopy* **108**, 29–42 (2007).

64. Giannozzi, P. et al. QUANTUM ESPRESSO: a modular and open-source software project for quantum simulations of materials. *J. Phys. Condens. Matter* **21**, 395502 (2009).